Growth of Solid Domains in Model Membranes: Quantitative Image Analysis Reveals a Strong Correlation between Domain Shape and Spatial Position

Uffe Bernchou,* John Hjort Ipsen, and Adam Cohen Simonsen

MEMPHYS Center for Biomembrane Physics, Department of Physics and Chemistry, University of Southern Denmark, Campusvej 55, DK-5230 Odense M, Denmark

The nucleation and growth of solid domains in supported bilayers composed of a binary mixture of equimolar 1,2-dioleoyl-sn-glycero-3-phosphocholine (DOPC) and 1,2-dipalmitoyl-sn-glycero-3-phosphocholine (DPPC) have been studied using combined fluorescence microscopy and AFM. We have found that the formation of the DPPC-enriched solid domains occurs by a combination of homogeneous and heterogeneous nucleation and that the nucleation density is directly proportional to the cooling rate. Furthermore, during cooling the shape of the domains evolve from compact to a branched morphology. This suggests that the growth is controlled by the diffusion of DPPC from the liquid phase toward the solid domain interface. In the late stages of the growth, we observe that the size and overall shape of the domains depend on the position of the nucleation points relative to the surrounding nucleation point positions. To analyze this effect, the nucleation points were used as generators in a Voronoi construction. Associated with each generator is a Voronoi polygon that contains all points closer to this generator than to any other. Through a detailed quantitative analysis of the Voronoi cells and the domains, we have found that their area, orientation, and asymmetry correlate and that the correlation becomes stronger for larger domains. This means that the spatial distribution of the nucleation points regulate the domain shape.

1. Introduction

Biological membranes are complex multicomponent macromolecular systems composed of a large number of lipid species and proteins.[1] The backbone of the membrane is the self-assembled lipid bilayer structure, which forms a quasi-two-dimensional cooperative system of 3–5 nm thickness. The membrane is composed by a variety of lipid species, which as pure components undergo an acyl chain melting transition with transition temperatures dependent on the molecular details. The lipid mixture of natural membranes can thus be described as a multidimensional complex phase diagram, for example, reflected in lateral phase coexistence with inhomogeneous membranes of spatially varying composition and structure. Lateral domain structure has for a long time been observed in synthetic and natural membranes[2] and supported theoretical works.[3]

In the raft hypothesis,[4] it was argued that the presence of lipid domains have a significant functional role in the biological membrane. The lipid rafts are glycospingolipid clusters enriched in cholesterol and glycosylphosphatidylinositol-anchored proteins.[5] These 10–200 nm highly dynamic domains are expected to compartmentalize specific cellular processes.[6] However, although intensely studied in the last two decades, the existence of rafts in cell membranes remains controversial, because their small size and fluctuating nature makes them hard to detect in vivo with any present experimental technique.[7]

Although elusive in cell membranes, lipid domains with raft-like properties have been found to coexist with liquid lipid regions in giant unilamellar vesicles (GUVs) formed from natural lipids extracted from brush border membranes, which are rich in sphingomyelin and cholesterol,[8] and also recently in giant plasma membrane vesicles obtained by chemically induced blebbing of cells.[9,10] Coexisting liquid phases have also been observed in native bovine pulmonary surfactant membranes[11] and red blood cell lipid monolayers.[12] Lipid solid domains have been visualized in human skin stratum corneum lipid membranes at physiological temperature and pH.[13]

To understand the physical principles governing domain formation in lipid membranes, model membranes with only a few components have been studied intensively in the last three decades. Phase coexistence has been observed in binary and ternary GUVs and planar supported bilayers. Coexisting liquid phases formed of ternary mixtures gives rise to circular domains through the action of line tension. Upon cooling into the phase coexisting region, the domains coarsen by a combination of diffusion as well as occasional coalescence of the domains.[14] In the case of solid/liquid phase coexistence, a multitude of different shapes of the solid domains have been reported.[15−28]

There are several physical effects that govern the overall shape of solid domains. Examples include the degree of line tension anisotropy, the interfacial activation energy barrier, the diffusion rates, the thermal history, and the equilibration time, and the complex interplay between these factors gives rise to the rich shape diversity. If the line tension is anisotropic due to crystalline anisotropy, lipid packing will influence the domain shape.[15,18] In this case the observed domains are often hexagonal or stripe-shaped.[15,18,19,23−25] For unequilibrated supercooled systems, the interfacial activation energy barrier determine whether the growth mode of the domains are reaction-limited or diffusion limited.[22] A high activation energy barrier leads to reaction-limited growth and compact circular domains, whereas a low activation energy barrier leads to diffusion-limited growth and fractal domains with a branched morphology.

Fractal domain shapes have been found in GUVs[23,24,19] and supported bilayers[22,28,29] of binary lipid mixtures. The formation of this type of patterning is typical in nonequilibrium crystal

---

* To whom correspondence should be addressed. Phone: +45 6550 3474; fax: +45 6550 4048; e-mail: uffe@memphys.sdu.dk.

Growth of Solid Domains in Model Membranes

J. Phys. Chem. B, Vol. 113, No. 20, 2009 **7171**

growth, where the stable phase propagates into the metastable supercooled phase, and the growth is controlled by the diffusion of the latent heat away from the interface.[30−32] However, lipid bilayers are surrounded by a large body of water, which absorbs the latent heat released during the phase transition, and the diffusion of heat is not the limiting factor. Binary mixtures containing a high melting and a low melting lipid component forms solid domains enriched in the high melting component when the system is cooled into the phase coexisting region. In this case the growth is controlled by the diffusion of the high melting component from the liquid phase toward the solid domain interface.

We have studied the nucleation and growth of solid domains in supported bilayers composed of a binary mixture of equimolar 1,2-dioleoyl-sn-glycero-3-phosphocholine (DOPC) and 1,2-dipalmitoyl-sn-glycero-3-phosphocholine (DPPC) using fluorescence microscopy. Supported bilayers allows the use of atomic force microscopy (AFM) to characterize nanoscale structures, and the planar geometry facilitates the quantitative analysis of fluorescence images. We have found that the formation of the DPPC-enriched solid domains occurs by a combination of homogeneous and heterogeneous nucleation and that the nucleation density is controlled by the cooling rate.

We observe that the size and overall shape of the domains depend on the position of the nucleation points relative to the surrounding nucleation point positions. To analyze this effect, the nucleation points were used as generators in a Voronoi construction. Associated with each generator is a Voronoi polygon that contains all points closer to this generator than any other.[33] The polygons create a segmentation of the entire surface such that each domain is surrounded by a polygon. In epitaxial island growth, the Voronoi polygon is the simplest and most conventional cell that describes a "capture zone" of adatoms for the corresponding island.[34] Such cells are used to explain experimentally observed epitaxial island area distributions.[34−37] Through detailed quantitative image analysis, we have found that not only the area but also the orientation and asymmetry of the domains correlate with the Voronoi polygons, which means that the spatial distribution of the nuclei positions regulate the domains shape.

2. Experimental Procedures

2.1. Materials. DPPC and DOPC were purchased from Avanti Polar Lipids and were used without further purification. 1,1′-Dioctadecyl-3,3,3′,3′-tetramethylindocarbocyanin perchlorate (DiI-C_{18}) was from Molecular Probes. Sodium phosphate, dibasic (>99%) and sodium phosphate, monobasic (>99%) were from Sigma, abd NaCl (>99.5%) was from Fluka. Methanol from Sigma and n-hexane from Fluka were HPLC grade quality, and ultra pure Milli-Q water (18.3MΩcm) was used in all steps involving water. Phosphate buffer (10 mM phosphate, 128 mM NaCl) was prepared at pH 7.0 by mixing the appropriate amounts of di- and monobasic sodium phosphate and has a ionic strength of 150 mM. Muscovite mica (75 mm × 25 mm × 200 μm sheets) was from Plano GmbH, Germany. Mica sheets of 10 × 10 mm were preglued onto round (0.17 mm, 24 mm) microscope coverslips using a transparent and biocompatible silicone glue (MED-6215, Nusil Technology, Santa Barbara, CA). Immediately prior to use, the mica was cleaved with a knife, leaving a thin and highly transparent mica film on the coverslip.

2.2. Preparation of Supported Lipid Bilayers. The preparation of supported membranes by hydration of spin-coated lipid films has been described and validated previously.[38,39] To prepare

a dry spin-coated lipid film on mica, we used a stock solution of 10 mM lipid mixture (1:1 molar ratio of DOPC and DPPC) containing 0.5% DiI-C_{18} in hexane/methanol (97:3 volume ratio). A droplet (30 μL) of this lipid stock solution was then applied to freshly cleaved mica and immediately thereafter spun on a Chemat Technology KW-4A spin-coater at 3000 rpm for 40 s. This creates a dry multilamellar lipid film where lipids in the distal monolayer have their acyl chains oriented outward. The sample was then placed under vacuum in a desiccator for 10−15 h to ensure complete evaporation of solvents. To hydrate the dry spincoated film, the sample was subsequently moved to the fluid cell (BioCell, JPK Instruments AG, Berlin, Germany). Phosphate buffer was added, and the immersed sample was heated to 55 °C for 1 h. The sample was then placed on the fluorescence microscope and flushed with 55 °C buffer using a pipet adjusted to 500 μL. By monitoring the response of the lipid film while washing, the removal of lipid layers can be accurately controlled. Typically, the center of the sample is flushed, and this completely removes all but the lowest bilayer in this region. After the washing procedure, the liquid volume was gently exchanged 5−10 times to remove membranes in solution.

2.3. Microscopy. *2.3.1. Epi-flourescence Microscopy.* A Nikon TE2000 inverted microscope with a 40× long working distance objective (Nikon, ELWD, Plan Fluor, NA = 0.6) was used for epifluorescence observations. Fluorescence excitation was done at 540 nm with a xenon lamp (PolychromeV, Till Photonics GmbH, Gräfelfing, Germany), and a G-2A filtercube (Nikon) appropriate for the DiI probe was used to select fluorescent light from the sample. Images were recorded with a high-sensitivity CCD camera (Sensicam em, 1004 × 1002 pixels, PCO-imaging, Kelheim, Germany) and operated with TILLvisION software (Till Photonics GmbH).

2.3.2. AFM Imaging. Atomic force microscopy was performed using a JPK Nanowizard AFM system (JPK Instruments AG) operated in contact mode. Silicon nitride cantilevers of the triangular type (MSCT, D-lever, Veeco) were used, with a nominal spring constant of 0.03 N/m and a resonance frequency of 15 kHz. During scanning, the sample was located in the fluid cell (BioCell, JPK Instruments AG) also used for fluorescence imaging.

2.4. Continuous Cooling Experiment. To observe domain nucleation and growth, samples were cooled continuously from high temperatures, where the lipid bilayer is in the liquid phase, to low temperatures, where solid phase domains coexist with the liquid phase. Samples were cooled at approximately 1 °C/min from 50 to 16 °C, and the temperature was recorded with the accuracy of 0.1 °C with the thermal sensor placed in the liquid cell very close to the surface of the sample. Images were recorded manually at approximately 10 s intervals, and the corresponding temperature was noted.

2.5. Image Analysis. AFM images were processed and analyzed using the scanning probe image processor (SPIP; Image Metrology, Hørsholm, Denmark).

Epi-fluorescence images were analyzed to extract information about the shape of the domains. To enhance domain boundaries, the fluorescence images were Fourier transform bandpass filtered using ImageJ software (ImageJ, National Institute of Health, USA). This process filters large structures down to 40 pixels and small structures up to 3 pixels. Further analysis was automated using custom m-files written in Matlab.

The analysis procedure extracts the information about all $i = 1−N$ domains in all $j = 1−M$ images, where $j = 1$ is the image recorded at the lowest temperature and $j = M$ is recorded
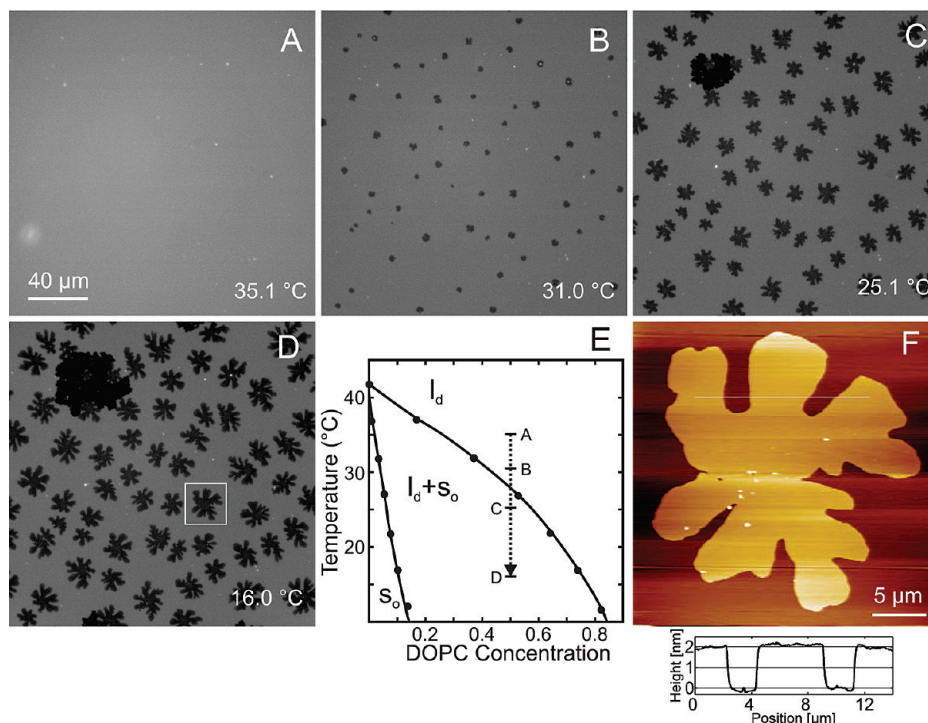
Figure 1. Selected fluorescence images recorded during a continuous cooling experiment displaying the nucleation and growth of solid domains from an initially liquid supported membrane composed of equimolar DOPC and DPPC. At 35.1 °C (A) the membrane is in the liquid state and the lipids are completely mixed. At 31 °C (B) DPPC rich domains nucleate and start to grow. A reduction of the molecular area during phase transition leads to the formation of a hole in the membrane (C). At 16 °C (D) the cooling is terminated and the domain growth stops. The temperatures where the four images were recorded is indicated in the temperature-composition phase diagram[41] of the mixture in panel E. (F) AFM image of the domain highlighted in panel D.

at the highest temperature. Initially, image $j = 1$ was segmented by conversion to a binary image by a cutoff approach. All domains containing less than 50 pixel were removed, leaving N domains. The development of domain i was then followed by cropping and segmenting image $j + 1$ using a modified bounding box of domain i in image j. The modification exists in expanding the bounding box by two pixels in all four direction. This procedure was repeated until image $j = j^*$, where the bounding box in image $j = j^* + 1$ was less than 25 pixels in width or height. The centroid of domain i in image j^* we define as the nucleation point of that domain. This means that the first image recorded where the domain is larger than 21 pixels in width or height is the first image analyzed with respect to that domain. The temperature at which this image is recorded we define as the nucleation point temperature of that domain. If the nucleation point was found to be within 15 pixels from the edge of the image, that domain was not further considered or analyzed. The procedure was repeated for all N domains.

3. Results and Discussion

3. 1 lipid Domain Formation and Growth. We investigate the formation and growth of solid domains when the lipid bilayer is cooled from the liquid phase into the phase coexisting region. The supported bilayers prepared above the fluidus line by the procedure described in Section 2.2 appears homogeneous and free of defects over large areas of the sample when visualized by fluorescence microscopy as seen in Figure 1A. This image and the following are images selected from a stack of images recorded in a continuous cooling experiment as described in Section 2.4. As the sample is cooled, solid domains start to nucleate at positions scattered across the surface as seen in Figure 1B. This nucleation process takes place at a very narrow temperature range of approximately 1 °C, and further cooling

does not generate new nuclei. Solid domains are identified in the images as the fluorescent probe partly is excluded from that phase. The domain nuclei appear initially small and rather compact, but by further lowering the temperature the domains grow in area and appear more fractal as seen in Figure 1C. The molecular area of lipids in the solid phase is typically smaller than lipids in the liquid phase.[40] The growth of the solid domains will, therefore, result in a reduction of the total area of the membrane, which for a supported bilayer will lead to the rupture of the membrane and the formation of holes as observed in Figure 1C. The hole is distinguished from solid domains by a lower fluorescence intensity. When further cooled, the hole grows to encircle the surrounding solid domains as seen in Figure 1D, which is recorded at 16 °C. At this temperature the solid domains have grown to occupy 30% of the membrane area. The temperatures where the four images were recorded is indicated in the temperature-composition phase diagram[41] of the mixture in Figure 1E. In general, for the four different samples we have investigated, the mean nucleation point temperature observed was 31.1 ± 1.0 °C, which is 3.0 °C higher than expected from the fluidus line in the diagram. However, Beattie et al. has measured an even higher transition temperature for this mixture in GUVs.[42] After reaching 16 °C, the temperature is fixed and the growth of the domains stops.

AFM was used to check for the presence of small domains below the optical resolution limit. Figure 1F shows an AFM image recorded 2 h after terminating the cooling process of the domain highlighted in Figure 1D. This image clearly displays the two phases. The hight difference of 2.2 ± 0.1 nm (linescan) of the phases is larger than typically measured height differences of ~1.2 nm[43] between solid and liquid domains. This discrepancy probably arises because the spincoated films prepared in salt conditions are more elevated from the support as compared
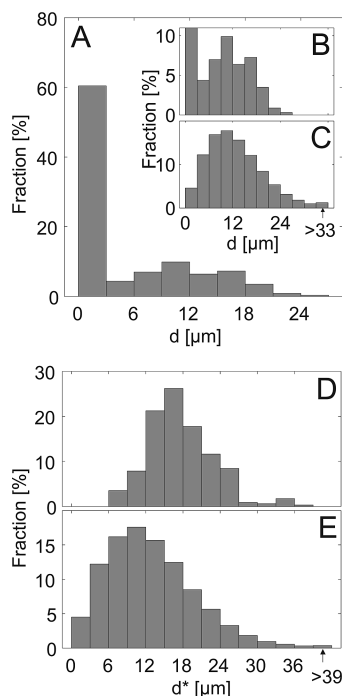
Growth of Solid Domains in Model Membranes

J. Phys. Chem. B, Vol. 113, No. 20, 2009 **7173**

Figure 2. Nearest neighbor nucleation point distances during a temperature cycle. The histogram in panel A shows the distance from a nucleation point in one cycle to the nearest nucleation point in the next cycle. Panel B is a zoom of panel A. The same histogram for randomly distributed points is shown in panel C. The histogram in panel D shows the distance from a nucleation point in one cycle to the nearest nucleation point in the same cycle. The same histogram for randomly distributed points is shown in panel E.

to supported bilayers prepared without using salt,[14] therefore the AFM needle will press the liquid bilayer to the mica surface even though the force is kept as low as possible. In general, the mica surface will interact with the zwitterionic head groups in the lower leaflet of the supported bilayer. It has been shown[14] that using physiological salt levels will reduce this interaction and induce a significant decoupling of the bilayer through electrostatic screening. The AFM image indicates that the domains have smooth edges on the micrometer length scale. Importantly, this comparison shows that there are no significant structural features of the domains that can not be obtained from the fluorescence images alone.

3.2. Domain Nucleation. To investigate if the nucleation of the domains is homogeneous or is defect mediated, a sample is repetitively cooled and heated at approximately 1 °C/min between 40 and 25 °C five times. After each cycle the temperature is held at 40 °C for 20 min to ensure homogeneous mixing of the lipids. The images from the five cycles were analyzed as described in Section 2.5. On average, 69 ± 5 nucleation points were observed per cycle. We measure the distance (d) from a nucleation point position in one cycle to the nearest nucleation point position in the next cycle. Figure 2A shows a histogram of d for all cycles. It is seen that 60.5% of the nucleations points are found within 3 μm of a nucleation point in the previous cycle. The bin width of 3 μm was chosen to best illustrate the significant features of the histogram. In figure 2 C is plotted a histogram of d that is generated by 1000 times randomly distributing 69 points over an area with the same size as the fluorescence image. Here it is seen that only 4.6% of the positions are found within 3 μm. This means that more than half of the nucleation processes are mediated by static defects in the bilayer or the underlying support. In Figure 2B, a fraction of the histogram in Figure 2A, focusing on distances

d beyond 3 μm, is shown. This part of the histogram resembles the histogram for random points very well, which is expected as the last 40% of the nucleation sites are not mediated by static defects, and the nucleation of these domains is uncorrelated with the previous nucleation positions.

We use the same set of data to investigate the correlation of nucleation point positions within the same cycle. We measure the distance from each nucleation point to the nearest nucleation point within the same cycle d^*. Figure 2D shows a histogram of d^* for all five cycles. Figure 2E is a histogram of d^* that is generated by 1000 times randomly distributing 69 points over an area with the same size as the fluorescence image. The difference between these histograms is very pronounced. The average distance between experimentally observed nearest neighbor nucleation points is 17.2 μm, whereas it is 12.9 μm for randomly distributed points. Furthermore, 16.2% of the randomly distributed points are located within a distance of 6 μm from their nearest neighbor, although no experimentally observed nearest neighbor nucleation points was found below 6 μm. These findings suggests that the nucleation point positions are correlated. In the following we will suggest a qualitative interpretation of this observation.

Upon nucleation and in the subsequent growth of a domain, a region with lowered DPPC concentration is located in the vicinity of the interface because the solid ordered phase is enriched in DPPC. In this depletion region, there will be a lower probability of creating new nuclei. Furthermore, a consequence of the reduction in the molecular area of lipids entering the solid phase is the build up of a tension in the membrane. This tension will ultimately lead to the rupture of the bilayer and to the generation of a membrane-spanning hole, as seen in Figure 1, panels C and D. Applying the Gibbs−Duhem equation for phase coexistence, $\mu_{\text{solid}}(T,\sigma) = \mu_{\text{liquid}}(T,\sigma)$, where σ is the tension, we can obtain a relation for the dependence of the melting temperature, T_m on the tension:

$$\frac{\mathrm{d}T_{\mathrm{m}}}{\mathrm{d}\sigma} = -\frac{a_{\text{liquid}} - a_{\text{solid}}}{\Delta H_{\mathrm{m}}} T_{\mathrm{m}} \tag{1}$$

where a_{liquid} and a_{solid} are molecular area of lipids in the liquid and solid state, respectively, and ΔH_{m} is the enthalpy of melting, which is positive. From this relation we can see that applying a tension to the membrane results in a lowered melting temperature. From classical nucleation theory,[21,44] we expect the activation barrier to nucleating a 2-dimensional (2D) bilayer disk to be

$$\Delta G^* = \frac{\pi \gamma^2 a_{\text{solid}}}{2\Delta H_{\mathrm{m}}} \frac{T_{\mathrm{m}}}{T_{\mathrm{m}} - T} \tag{2}$$

where γ is the interfacial line tension. The steady state nucleation rate, J, is given by $J = k \exp(-\Delta G^*/k_B T)$, where k_B is the Boltzmann constant, and k is a pre-exponential rate constant. From this relation, we expect the nucleation rate to be reduced if the melting temperature is lowered. Applying a tension to the membrane thus leads to a reduction in the nucleation rate. Depletion and tension will, therefore, both result in an increased distance between nearest neighbor nucleation points and may explain the observed nucleation pattern. The distance from the interface where these effects apply is unknown, but we are currently developing a quantitative model that will clarify such issues. Depletion and tension in the membrane also accounts
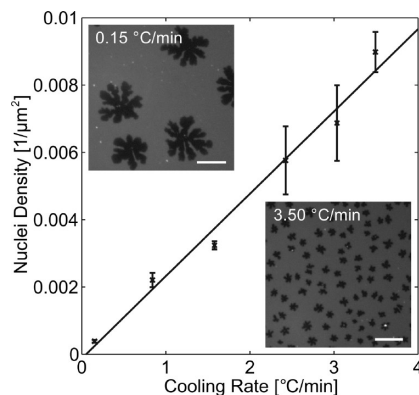
Figure 3. Nuclei density measured as a function of cooling rate. A linear least-squares fit is shown. The bars in the inserts are 20 μm.

for the observation that nucleation is terminated very rapidly after entering the phase coexistence region during cooling.

To study how the density of nuclei is affected by the cooling rate, samples were cooled at specific cooling rates from 40 to 25 °C. The temperature in the liquid cell very close to the surface of the membrane was logged at 2 s intervals. Images were recorded at 4 different locations on the sample after reaching 25 °C, and the average nuclei density was noted. In the temperature interval where nucleation occurs, the temperature was plotted as a function time, and the slope of the plot was used to determine the exact cooling rate. Figure 3 shows a plot of the nuclei density as a function of the cooling rate in the interval between 0.15 °C/min and 3.50 °C/min. As seen from the plot, the nuclei density increases almost linearly with cooling rate in this interval, and the density is 20-fold higher at 3.50 °C/min than at 0.15 °C/min. The insets in the figure are representative images at these two cooling rates. A linear least-squares fit is shown in the plot. The fit has a slope of $0.0025 \pm 0.0004(1)/(\mu m^2)(min)/(°C)$. From relation 2, it is seen that the activation barrier to nucleating a solid domain is inversely proportional to the degree of supercooling, $\Delta T = T_m - T$. In another study of lipid domain formation,[21] the nucleation rate was measured as a function of the degree of supercooling. We have found it difficult to supercool our system, because nucleation is observed to occur immediately after cooling the sample to temperatures lower than approximately 31 °C, even at our highest attainable cooling rate. However, our method for determining the nucleation point temperature is rather uncertain, especially at high cooling rates, and, therefore, it is possible that some degree of supercooling is obtained. To clarify these issues, future experiments should be conducted using a higher frame rate, which will give a more accurate value for the nucleation point temperature. It is not obvious from classical nucleation theory, how the nucleation density should depend on the cooling rate, but we hope that our future modeling will relate these parameters.

3.3. Quantitative Domain Shape Analysis. 3.3.1. Fundamentals. We will now give a detailed quantitative analysis of the lipid domains in terms of shape, area, position and orientation. To collect sufficient statistics, four different samples were investigated. The cooling of these samples produces structures similar to those seen in figure 1 B-D, and the images from all four experiments were analyzed as described in section 2.5.

It is clear from the images in figure 1 C and D, that there is a distribution of sizes of the solid domains. Apparently, domains that are positioned closer together are smaller than domains that are positioned far from each other. A similar effect is observed
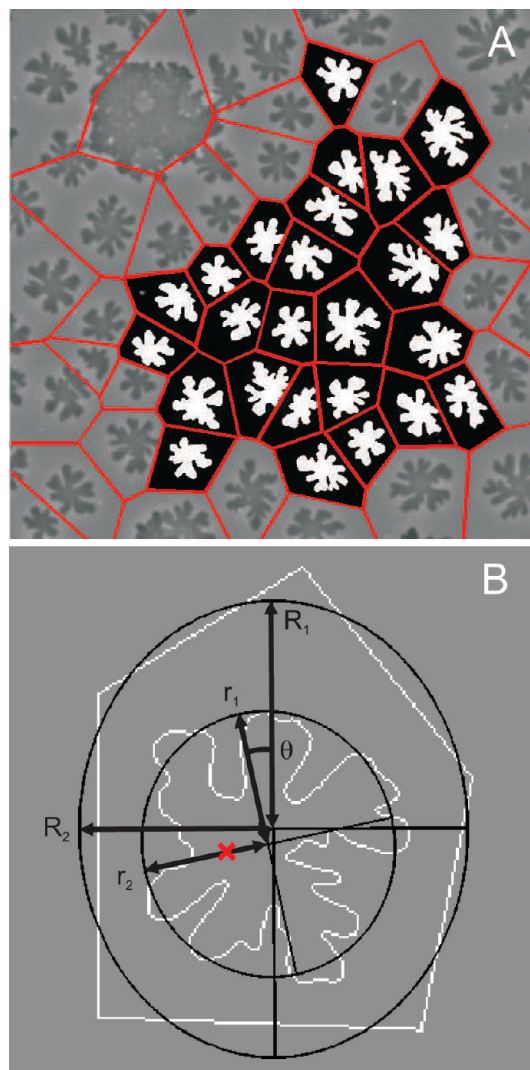

Figure 4. Domain shape analysis. (A) The Voronoi diagram constructed from the nucleation points is shown in red. Manually chosen domains are segmented and are shown in white, and their corresponding Voronoi polygons are shown in black. (B) The edges of a domain and the corresponding Voronoi polygon are shown in white. The ellipse of gyration of the domain and the polygon are shown in black. The nucleation point of the domain is shown in red.

in epitaxial growth of islands on surfaces.[35] Here it is observed that individual islands grow at a rate proportional to the size of their "capture zone".[36] The capture zone of an island is a 2-dimensional region of the sample from which adatoms are more likely to diffuse to this island than any other.[37] For heterogeneous nucleation, it has been demonstrated that the capture zones are closely approximated by the Voronoi polygons for each nucleation site.[36] This seems reasonable as the Voronoi polygons identifies a region that contains all points closer to the corresponding nucleation point than any other.[33] In fact, numerical studies of the diffusion equation with appropriate boundary conditions for simple island configurations show that the Voronoi polygon walls are very close to the lines of zero monomer flux.[36]

The Voronoi diagram associated with the lipid bilayer presented in figure 1 A-D is seen in red in figure 4 A. We have omitted domains close to edges of the image and holes in the bilayer in the further investigation. In figure 4 A, the investigated domains are highlighted in white with the corresponding
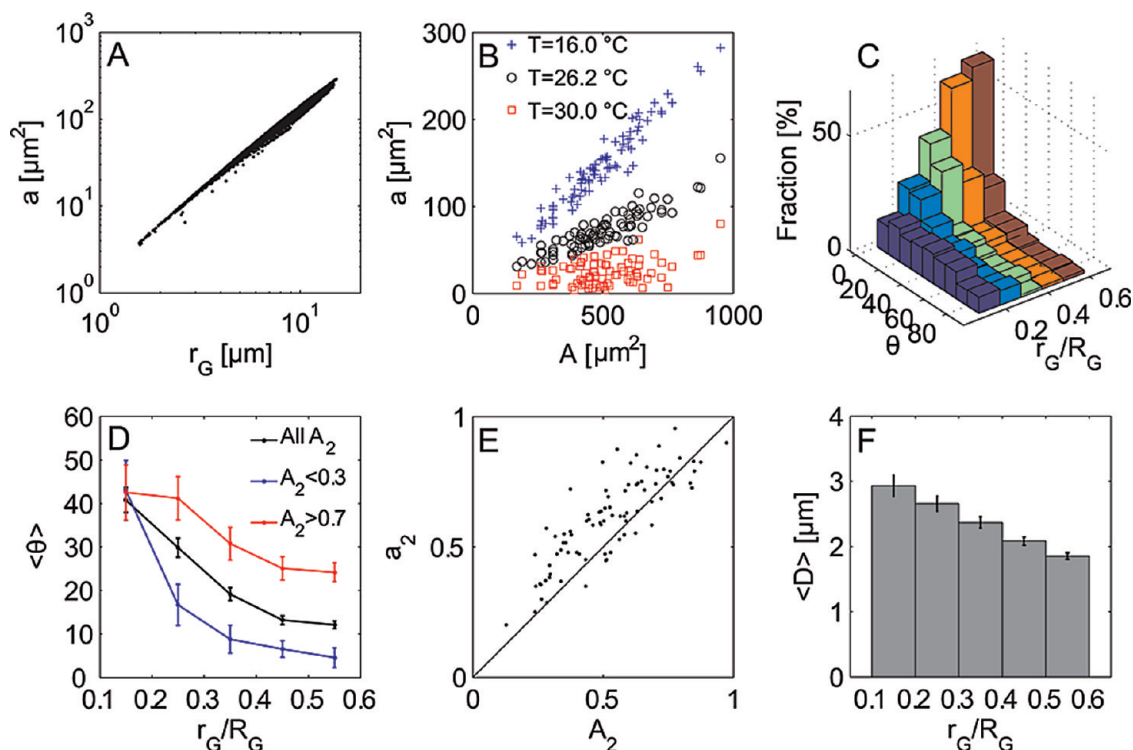
Figure 5. Quantitative analysis of the fluorescence images. (A) log−log plot of the domain area vs radius of gyration. (B) The domain area vs Voronoi polygon area is plotted for three different temperatures. (C) The distribution of θ is plotted as a function of the size ratio. (D) $\langle \theta \rangle$ is plotted as a function of the size ratio for different Voronoi polygon asymmetries. The error bars signify 95% confidence intervals assuming a normal distribution of the data. (E) Domain asymmetry vs Voronoi polygon asymmetry is plotted for images recorded at 16 °C. (F) The mean distance from the center of mass of a domain to the center of mass of the corresponding Voronoi polygon is plotted as a function of the size ratio. Again, the error bars signify 95% confidence intervals assuming a normal distribution of the data.

Voronoi polygons in black. We use the binary image of each domain to calculate the gyration tensor[45]

$$t = \begin{pmatrix} \langle x^2 \rangle - \langle x \rangle^2 & \langle xy \rangle - \langle x \rangle \langle y \rangle \\ \langle xy \rangle - \langle x \rangle \langle y \rangle & \langle y^2 \rangle - \langle y \rangle^2 \end{pmatrix} \quad (3)$$

where x and y are the positions of the pixels in the domain and the averages are over all pixels in one domain. This tensor can be diagonalized by rotation through an angle $\phi = (1/2)\arctan((2t_{xy})/(t_{xx} - t_{yy}))$. The principal radii of gyration of the domain are the eigenvalues of the tensor,

$$r_1^2, r_2^2 = \frac{1}{2}\left(t_{xx} + t_{yy} \pm \sqrt{(t_{xx} + t_{yy})^2 + 4t_{xy}^2}\right) \quad (4)$$

and the radius of gyration is $r_G^2 = r_1^2 + r_2^2$. The asymmetry of the domain we define as the ratio of the smaller to the larger principal radius of gyration squared $a_2 = r_2^2/r_1^2$, which means that linear domains have $a_2 = 0$ and circular domains have $a_2 = 1$. The principal radii of gyration can be illustrated by the ellipse of gyration, an ellipse of semi axes r_1 and r_2, oriented at an angle ϕ with the horizontal, and centered on the center of mass of the domain. This is shown in Figure 4 B for the domain highlighted in Figure 1D. Similarly, for the Voronoi polygons we can define the principal radii of gyration, R_1 and R_2; the orientation of the ellipse of gyration with the horizontal, Φ; the radius of gyration, R_G; and asymmetry, A_2. We can now define the alignment angle, $\theta = |\phi - \Phi|$ between the ellipse of gyration of the domain and the corresponding Voronoi polygon.

3.3.2. Results. To investigate the fractality of the domains, the area, a, versus radius of gyration is plotted in a log−log

plot in Figure 5 A. This plot contains data from all images of all 84 investigated domains, giving 4021 data points. Fitting a power law $a \propto r_G^\alpha$ to all data points gives a value of the fractal dimension $\alpha = 1.79 \pm 0.01$. This value is statistically significantly smaller than 2, which is expected for compact domains, but is slightly larger than 1.71, which is found for diffusion-limited aggregation (DLA) clusters.[31] It should be noted that the measured fractal dimension is the average quantity for all domains at all temperatures. At high temperatures, the fractal dimension will naturally be closer to 2, as the domains are more compact, and likewise the fractal dimension at low temperatures will be lower than 1.79, but no discrete shape transition from compact to fractal morphology is observed in the plot.

The effect of the position of the nearest neighbors on the growth of the domains is now investigated. In Figure 5B the domain area versus Voronoi polygon area, A, is plotted for three different temperatures. At 30 °C the domain area is weakly correlated with the Voronoi polygon area. The degree of correlation can be estimated by the area correlation coefficient defined by eq 5,

$$C(a, A) = \frac{\langle (a - \langle a \rangle)(A - \langle A \rangle) \rangle}{\sqrt{\langle a^2 - \langle a \rangle^2 \rangle}\sqrt{\langle A^2 - \langle A \rangle^2 \rangle}} \quad (5)$$

which gives 1 for perfectly correlated data and 0 for uncorrelated data. At 30 °C the area correlation coefficient is 0.40. When the temperature is lowered to 26.2 °C the date points in the plot are a lot more correlated, which is confirmed by an area correlation coefficient of 0.90. This trend is followed as the temperature is lowered to 16.0 °C, where the area coefficient is

increased to 0.97. This means that when the domains grow large, their areas are completely accounted for by the positions of the nearest neighbors.

It is clear from Figure 1D that the domains are not expanding homogeneously in all directions. We can investigate whether the nearest neighbor positions control the directions in which the domains grow. If this is the case, the semi-axes of the ellipse of gyration of the domain would aline along the semi-axes of the ellipse of gyration of the corresponding Voronoi polygon. This means that the alignment angle would approach 0, as the domains grow. This is demonstrated in Figure 5C, where the distribution of θ is plotted as a function of the ratio of the radius of gyration of domains and the radius of gyration of the corresponding polygons, here termed the size ratio, $\Gamma = r_G/R_G$. For small size ratios, which means for small domains compared to polygon areas, the alignment angle is evenly distributed between 0 and 90°. This is expected for domain growth not controlled by nearest neighbor positions. But as the domains grow, and Γ approaches unity, it is clearly demonstrated in the plot, that θ approaches 0. This means that the direction of domain growth is controlled by the position of the nearest neighbors.

Some of the Voronoi polygons are not very elongated and have asymmetries close to 1. For such polygons the semi-axes of the ellipse of gyration are almost arbitrarily oriented, and the direction of growth of the corresponding domains would not be controlled strongly by the nearest neighbors. On the other hand, very asymmetric Voronoi polygons would facilitate directional growth more strongly. To investigate this hypothesis, we plot the mean alignment angle $\langle\theta\rangle$ between the ellipse of gyration of the domain and the corresponding Voronoi polygon as a function of the size ratio in Figure 5D. In this figure, the histogram shown in black is based on analysis of all domains, the histogram in red is based on domains where the corresponding Voronoi polygon has an asymmetry larger than 0.7, which is for compact polygons, and the histogram in blue is based on domains where the corresponding Voronoi polygon has an asymmetry smaller than 0.3, which is for elongated polygons. These histograms illustrates that the growth of domains with elongated corresponding Voronoi polygons is more strongly controlled by the nearest neighbor positions on average than the growth of domains inside compact Voronoi polygons. It is also seen that elongated Voronoi polygons strongly align the corresponding domains already at size ratios ranging from 0.2 to 0.3, where domains with compact corresponding Vororoi polygons are oriented almost randomly.

As the asymmetry of the Voronoi polygons control the direction of the domain growth, it would be interesting to investigate if asymmetric polygons lead to asymmetric domains. The degree of correlation can be estimated from the asymmetry correlation coefficient, which is defined similar to eq 5 with a and A replaced by a_2 and A_2, respectively. The domain asymmetry versus Voronoi polygon asymmetry is plotted in Figure 5E for $T = 16.0\,°C$. At this temperature, the symmetry correlation coefficient is 0.84. This means that the domains have asymmetries that approach the Voronoi polygon asymmetries. However, as seen from the plot, most data points are located above the diagonal, which means that almost none of the domains are as asymmetric as the corresponding Voronoi polygons.

As the domains do not grow uniformly in all directions, the center of mass of the domains may change position during the growth process. The Voronoi polygons apparently control the area, orientation, and asymmetry of the domains. Therefore,

it is likely that the domain center of mass moves toward the center of mass of the corresponding Voronoi polygon. To investigate if this is the case, we plot the mean distance from the center of mass of the domain to the center of mass of the corresponding Voronoi polygon, $\langle D\rangle$, as a function of the size ratio in Figure 5F. It is seen from this figure that $\langle D\rangle$ is lowered from 2.9 ± 0.2 to $1.9 \pm 0.05\ \mu m$ during growth. This means that, on average, the domain center of mass is approaching the corresponding Voronoi polygon center of mass.

3.3.3. Discussion. We have now demonstrated that the shape of solid domains in supported binary lipid bilayers grown by diffusion is strongly controlled by the nucleation positions, especially in the late stages of the growth. We have characterized the effect of the positions of the nucleation points on the shape of the domains by comparing the evolution of the domains with the corresponding Voronoi polygons. It is observed that the area, orientation, and asymmetry of the domains correlate with the Voronoi polygons and that the center of mass of the domain is shifted from the nucleation point and toward the center of mass of the polygon. We can therefore envision the polygons as templates for the expansion of the domains. Diffusive growth apparently promotes the domains to fill the space defined by the polygons.

It would be interesting to investigate the development of the process as the size ratio approaches unity. However, this is not experimentally feasible. If we choose a higher DPPC to DOPC ratio, the phase diagram in Figure 1E predicts that we will achieve a larger solid domain area fraction. Our initial investigations using this approach resulted in a highly fractured membrane with numerous holes. As the analysis of the domain shape should be avoided near such defects, the approach was abandoned. Another procedure could be to simulate the process. In the future, it would be interesting to see if our observations could be reproduced and new effects predicted by simple DLA simulations. Such simulations could be conducted using experimentally observed, as well as randomly generated, seed positions. As we discussed previously, the observed nucleation points are correlated. Wether this correlation plays a critical effect for the domain shape could thereby be investigated.

Because the nucleation points control the shape of the domains, we may potentially direct the shape pattern in supported lipid bilayers in general by controlling the positions where nucleation occurs. Such structures could find technological relevance within supported lipid bilayer sensor applications.[46] As we discussed in Section 3.2, more than half of the nucleation events are mediated by static defects in the bilayer or the underlying support. The nature of these defects is presently unknown. If we can manufacture impurities with a stronger ability to promote nucleation than the naturally occurring defects, we may have a tool to control the nucleation pattern. Applicable techniques for the manufacturing of such nucleation centers include dip-pen nanolithography[47] and microcontact printing.[48]

As noted Section 3.3.1, it is a well-known observation in epitaxial growth that area distributions are effected by the nucleation process. To our knowledge, our study is the first to correlate the overall shape of objects grown by diffusion with the nucleation positions. Our findings could potentially be important in a range of applications within diffusive growth phenomena, including epitaxial island growth, electrodeposition,[49] bacteria growth under reduced food supply,[32,50] and growth of supported solid alkane domains.[51,52] Furthermore, the

Growth of Solid Domains in Model Membranes

J. Phys. Chem. B, Vol. 113, No. 20, 2009 **7177**

formation and growth of domains in biological membranes might have characteristics analogous to the findings described here.

References and Notes

(1) Genneis, R. B. *Biomembranes, Molecular Structure and Function*; Springer Verlag: London, 1989.

(2) Hartmann, W.; Galla, H.-J.; Sackmann, E. *FEBS Lett.* **1977**, *78*, 169–172.

(3) Ipsen, J.; Karlström, G.; Mouritsen, O. G.; Wennerström, H.; Zuckermann, M. J. *Biochim. Biophys. Acta* **1987**, *905*, 162–172.

(4) Simons, K.; Ikonen, E. *Nature* **1997**, *387*, 569–572.

(5) Brown, D. A.; Rose, J. K. *Cell* **1992**, *68*, 533–544.

(6) Pike, L. J. *J. Lipid Res.* **2006**, *47*, 1597–1598.

(7) Jacobson, K.; Mouritsen, O. G.; Anderson, R. G. W. *Nat. Cell Biol.* **2007**, *9*, 7–14.

(8) Dietrich, C.; Bagatolli, L. A.; Volovyk, Z. N.; Thompson, N. L.; Levi, M.; Jacobson, K.; Gratton, E. *Biophys. J.* **2001**, *80*, 1417–1428.

(9) Baumgart, T.; Hammond, A. T.; Sengupta, P.; Hess, S. T.; Holowka, D. A.; Baird, B. A.; Webb, W. W. *Proc. Natl. Acad. Sci. U. S. A.* **2007**, *104*, 3165–3170.

(10) Sengupta, P.; Hammond, A.; Holowka, D.; Baird, B. *Biochim. Biophys. Acta, Biomembr.* **2008**, *1778*, 20–32.

(11) de la Serna, J. B.; Perez-Gil, J.; Simonsen, A. C.; Bagatolli, L. A. *J. Biol. Chem.* **2004**, *279*, 40715–40722.

(12) Keller, S. L.; Pitcher III, W. H.; Huestis, W. H.; McConnell, H. M. *Phys. Rev. Lett.* **1998**, *81*, 5019–5022.

(13) Plasencia, I.; Norlen, L.; Bagatolli, L. A. *Biophys. J.* **2007**, *93*, 3142–3155.

(14) Jensen, M. H.; Morris, E. J.; Simonsen, A. C. *Langmuir* **2007**, *23*, 8135–8141.

(15) Gordon, V. D.; Beales, P. A.; Zhao, Z.; Blake, C.; MacKintosh, F. C.; Olmsted, P. D.; Cates, M. E.; Egelhaaf, S. U.; Poon, W. C. K. *J. Phys.: Condens. Matter* **2006**, *18*, L415–L420.

(16) Beales, P. A.; Gordon, V. D.; Zhao, Z. J.; Egelhaaf, S. U.; Poon, W. C. K. *J. Phys.: Condens. Matter* **2005**, *17*, S3341–S3346.

(17) Scherfeld, D.; Kahya, N.; Schwille, P. *Biophys. J.* **2003**, *85*, 3758–3768.

(18) Korlach, J.; Schwille, P.; Webb, W. W.; Feigenson, G. W. *Proc. Natl. Acad. Sci. U. S. A.* **1999**, *96*, 8461–8466.

(19) Li, L.; Cheng, J. X. *Biochemistry* **2006**, *45*, 11819–11826.

(20) Fidorra, M.; Duelund, L.; Leidy, C.; Simonsen, A. C.; Bagatolli, L. A. *Biophys. J.* **2006**, *90*, 4437–4451.

(21) Blanchette, C. D.; Lin, W. C.; Orme, C. A.; Ratto, T. V.; Longo, M. L. *Langmuir* **2007**, *23*, 5875–5877.

(22) Blanchette, C. D.; Orme, C. A.; Ratto, T. V.; Longo, M. L. *Langmuir* **2008**, *24*, 1219–1224.

(23) Bagatolli, L. A.; Gratton, E. *Biophys. J.* **2000**, *79*, 434–447.

(24) Bagatolli, L. A.; Gratton, E. *Biophys. J.* **2000**, *78*, 290–305.

(25) Leidy, C.; Kaasgaard, T.; Crowe, J. H.; Mouritsen, O. G.; Jorgensen, K. *Biophys. J.* **2002**, *83*, 2625–2633.

(26) Kaasgaard, T.; Leidy, C.; Crowe, J. H.; Mouritsen, O. G.; Jorgensen, K. *Biophys. J.* **2003**, *85*, 350–360.

(27) Giocondi, M. C.; Vie, V.; Lesniewska, E.; Milhiet, P. E.; Zinke-Allmang, M.; Le Grimellec, C. *Langmuir* **2001**, *17*, 1653–1659.

(28) Szmodis, A. W.; Blanchette, C. D.; Levchenko, A. A.; Navrotsky, A.; Longo, M. L.; Orme, C. A.; Parikh, A. N. *Soft Matter* **2008**, *4*, 1161–1164.

(29) Moran-Mirabal, J. A.; Aubrecht, D. A.; Craighead, H. G. *Langmuir* **2007**, *23*, 10661–10671.

(30) Brener, E.; Müller-Krumbhaar, H.; Temkin, D. *Phys. Rev. E: Stat., Nonlinear, Soft Matter Phys.* **1996**, *54*, 2714–2722.

(31) Sander, L. M. *Contemp. Phys.* **2000**, *41*, 203–218.

(32) Benjacob, E.; Garik, P. *Nature* **1990**, *343*, 523–530.

(33) Aurenhammer, F. *Comput. Surv.* **1991**, *23*, 345–405.

(34) Bartelt, M. C.; Stoldt, C. R.; Jenks, C. J.; Thiel, P. A.; Evans, J. W. *Phys. Rev. B: Condens. Matter Mater. Phys.* **1999**, *59*, 3125–3134.

(35) Evans, J. W.; Thiel, P. A.; Bartelt, M. C. *Surf. Sci. Rep.* **2006**, *61*, 1–128.

(36) Mulheran, P. A.; Blackman, J. A. *Philos. Mag. Lett.* **1995**, *72*, 55–60.

(37) Mulheran, P. A.; Blackman, J. A. *Phys. Rev. B: Condens. Matter Mater. Phys.* **1996**, *53*, 10261–10267.

(38) Simonsen, A. C.; Bagatolli, L. A. *Langmuir* **2004**, *20*, 9720–9728.

(39) Simonsen, A. C.; Jensen, U. B.; Hansen, P. L. *J. Colloid Interface Sci.* **2006**, *301*, 107–115.

(40) Nagle, J. F.; Tristram-Nagle, S. *Biochim. Biophys. Acta, Reviews on Biomembranes* **2000**, *1469*, 159–195.

(41) Elliott, R.; Katsov, K.; Schick, M.; Szleifer, I. *J. Chem. Phys.* **2005**, *122*, 044904.

(42) Beattie, M. E.; Veatch, S. L.; Stottrup, B. L.; Keller, S. L. *Biophys. J.* **2005**, *89*, 1760–1768.

(43) Burns, A. R. *Langmuir* **2003**, *19*, 8358–8363.

(44) Papon, P.; Leblond, J.; Meijer, P. H. E. *The Physics of Phase Transitions − Concepts and Applications*; Springer: Heidelberg, 2002.

(45) Saxton, M. J. *Biophys. J.* **1993**, *64*, 1766–1780.

(46) Castellana, E. T.; Cremer, P. S. *Surf. Sci. Rep.* **2006**, *61*, 429–444.

(47) Piner, R. D.; Zhu, J.; Xu, F.; Hong, S.; Mirkin, C. A. *Science* **1999**, *283*, 661–663.

(48) Xia, Y.; Whitesides, G. M. *Angew. Chem., Int. Ed.* **1998**, *37*, 550–575.

(49) Grier, D.; Benjacob, E.; Clarke, R.; Sander, L. M. *Phys. Rev. Lett.* **1986**, *56*, 1264–1267.

(50) Fujikawa, H.; Matsushita, M. *J. Phys. Soc. Jpn.* **1989**, *58*, 3875–3878.

(51) Riegler, H.; Kohler, R. *Nat. Phys.* **2007**, *3*, 890–894.

(52) Kohler, R.; Lazar, P.; Riegler, H. *Appl. Phys. Lett.* **2006**, *89*, 241906.